Square Wave Anodic Stripping Voltammetry at Mercury-Plated Electrodes. Simulation of Surface Morphology Effects on Electrochemically Reversible, Irreversible, and Quasi-reversible Processes: Comparison of Thin Films and Microdroplets

Matthew Powell, Jon C. Ball, Yu-Chen Tsai, Marco F. Suárez, and Richard G. Compton*

Physical and Theoretical Chemistry Laboratory, Oxford University, South Parks Road, Oxford, OX1 3QZ, United Kingdom

Mercury electroplated onto solid electrodes is widely used for electrochemical measurements. Depending on the substrate, the coating can take the form of either a uniform thin film or an assembly of microdroplets. It is interesting to ask the extent to which the morphological state can influence the nature of voltammetric responses from such electrodes. Accordingly, a general approach is developed for the numerical simulation of square wave anodic stripping voltammetry at hemispherical and uniform planar electrodes based on the backward implicit method. This is applied to the modeling of electrochemically reversible, irreversible, and quasi-reversible redox couples. Data from the simulations are validated by comparison of characteristic properties of the voltammograms with published work for the reversible limit of the planar electrode. The variation of these characteristic features with electrode geometry and electrode kinetics is studied, and a comparison between the planar and hemispherical geometry made. Last, experimental data is presented for the nature of mercury on the surface of both iridium and copper substrates, obtained by atomic force microscopy.

Introduction

There are numerous reports about the nature of mercury thin films (MTFs) on a range of electrode materials. Literature[1–3] is especially prevalent for mercury on glassy-carbon electrodes (GCEs). Štulíková[1] has shown that the manner in which the mercury is deposited affects the nature of the film, ranging from large mercury drops at relatively large separations to a wider distribution of smaller mercury droplets. Furthermore, upon electrode drying, mechanical joining of fine drops occurs. The work of Wu[2] supports the view that larger, more dispersed droplets occur under certain conditions, although it disagrees with Štulíková's[1] explanation of how they are formed, emphasizing their association with a transformation, resulting from, for example, evaporation of water from the surface and also as a result of surface perturbation of rapid potential changes under the anodic stripping voltammetry (ASV) condition. Zakharchuk and Brainina[3] also show evidence that microdroplets coalesce giving a few large (>10 μm) droplets.

The experimental papers[1–3] support the tendency of MTF coatings on GCEs to exist in a state of larger microdroplets, typically of the order of 1 μm in diameter, but up to >10 μm depending on the treatment. Whether this is due to a transformation to a more stable state triggered by various surface perturbations[2,3] or whether this is their initial state[1] is uncertain.

The formation of droplets is not, however, limited to MTFs on GCEs. Evidence including visualization via atomic force microscopy for mercury droplets on platinum, ranging from submicron to ca. 6 microns in diameter can be found in the literature.[4,5] Mercury can also be electroplated on iridium giving rise to a uniform film or hemispherical coverage.[6,7]

These observations have lead Štulíková[1] to note the need for a refined theoretical treatment of ASV at a MTF on GCEs that treats the surface as a large number of spherical drops rather than a thin, homogeneous mercury film.

This paper develops the theory of ASV via square wave voltammetry for the case of quasi-reversible electrode kinetics considering the electrode both as a uniform thin film experiencing semiinfinite linear diffusion and as an isolated droplet to which mass transport occurs via hemispherical diffusion. The behavior of the two are contrasted particularly in the limit of drops of small radius where the enhanced mass transport displays a significant effect on the apparent electrochemical reversibility of the redox couple under investigation. We additionally report experimental atomic force microscopy (AFM) data for mercury deposited on copper and iridium substrates to complement the data already reported for GCEs (see above) and further illustrate the need for some caution in the application of linear diffusion theory based on the thin film assumption to MTF electrodes.

Theory

We examine the following redox reaction

$$\text{RED(amalgam)} \underset{k_b^a}{\overset{k_a}{\rightleftharpoons}} \text{OX(aq)} + 2e^-$$
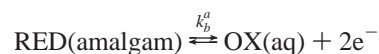
which is first considered to occur at the surface of a hemispherical mercury electrode, where k_b^a is the apparent rate constant for the reduction (back) reaction. The net flux at the electrode surface is given by[8]

$$j = -k_b^a\{[\text{OX}] - [\text{RED}]e^\theta\} \tag{1}$$

where

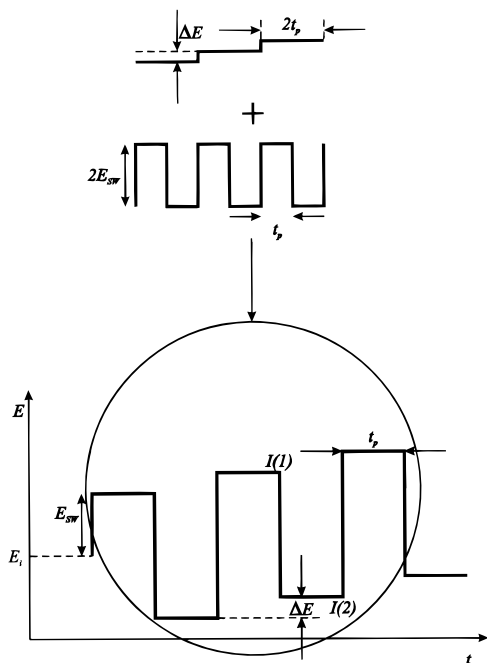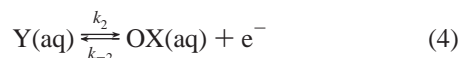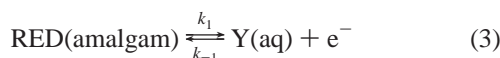$$\theta = \frac{2F}{RT}(E - E^{\circ\prime}) \tag{2}$$

Figure 1. Schematic diagram showing a square wave voltammetric sweep.

E is the potential of the square wave scan and $E^{\circ\prime}$ the formal potential of the redox couple. The two-electron process takes place in two steps[8]

$$\text{RED(amalgam)} \underset{k_{-1}}{\overset{k_1}{\rightleftharpoons}} \text{Y(aq)} + \text{e}^- \qquad (3)$$

$$\text{Y(aq)} \underset{k_{-2}}{\overset{k_2}{\rightleftharpoons}} \text{OX(aq)} + \text{e}^- \qquad (4)$$

where Y is an intermediate. If the first step is rate determining[8]

$$k_b^a = A_1 \exp(-{}^1\!/_2(1 + \alpha_1)\theta) \qquad (5)$$

whereas if the second step is rate determining[8]

$$k_b^a = A_1 \exp(-{}^1\!/_2\alpha_2\theta) \qquad (6)$$

where A_1 is a constant for a particular reaction and α_1 and α_2 are the Tafel coefficients describing the individual electron transfer steps.

In square wave ASV, the electrode is subjected to the square wave voltammetric sweep where E changes as shown in Figure 1, where ΔE is the step voltage of the staircase, E_{SW} is the pulse amplitude, E_i is the starting voltage for the scan, and t_p is period of the pulse. During the square wave experiment the current flowing is measured at the points shown for each pulse; $I(1)$ is known as the forward current and $I(2)$ as the backward current. The difference current

$$\Delta I = I(1) - I(2) \qquad (7)$$

is recorded and plotted against the average potential of the corresponding forward and backward pulses.

RED and OX are both assumed kinetically stable, and initially only RED is present in the mercury electrode at a concentration of $[\text{RED}]_{t=0}$. No reduced species is presumed to exist in the solution, nor any oxidized species in the mercury electrode.

Time-dependent mass transport equations for both species are given by Fick's second law. These are given as a function
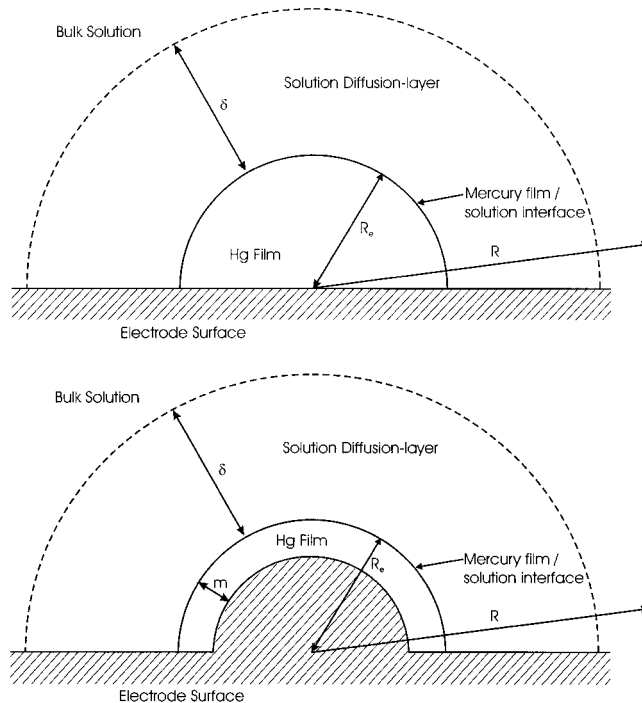

Figure 2. Schematic diagram showing coordinates and principal dimensions of (a, top) the hemispherical system and (b, bottom) the inert centered system.

of the radial coordinate, R (Figure 2a), to take advantage of the symmetry of the hemispherical system.[9]

$$\frac{\partial a}{\partial t} = D_a\left\{\frac{\partial^2 a}{\partial R^2} + \frac{2}{R}\frac{\partial a}{\partial R}\right\} \qquad (8)$$

$$\frac{\partial b}{\partial t} = D_b\left\{\frac{\partial^2 b}{\partial R^2} + \frac{2}{R}\frac{\partial b}{\partial R}\right\} \qquad (9)$$

where D_a and D_b are respectively the applicable diffusion coefficients for the reduced and oxidized species, and a and b are defined as follows

$$a = [\text{RED}]/[\text{RED}]_{t=0} \qquad (10)$$

The introduction of a new coordinate,[10] ψ, where

$$b = [\text{OX}]/[\text{RED}]_{t=0} \qquad (11)$$

$$\psi = 1 - \frac{R_e}{R} \qquad (12)$$

and R_e is the electrode radius, transforms mass transport eq 9 to

$$\frac{\partial b}{\partial t} = D_b\left(\frac{(1-\psi)^2}{R_e}\right)^2\frac{\partial^2 b}{\partial \psi^2} \qquad (13)$$

which is valid for $0 \leq \psi < 1$ (where $R \geq R_e$). This transformation is computationally efficient as it distorts space such that there is a higher density of node points close to the electrode surface, where there is a maximum variation in concentrations (see Figure 3).

For the reduced species we introduce φ

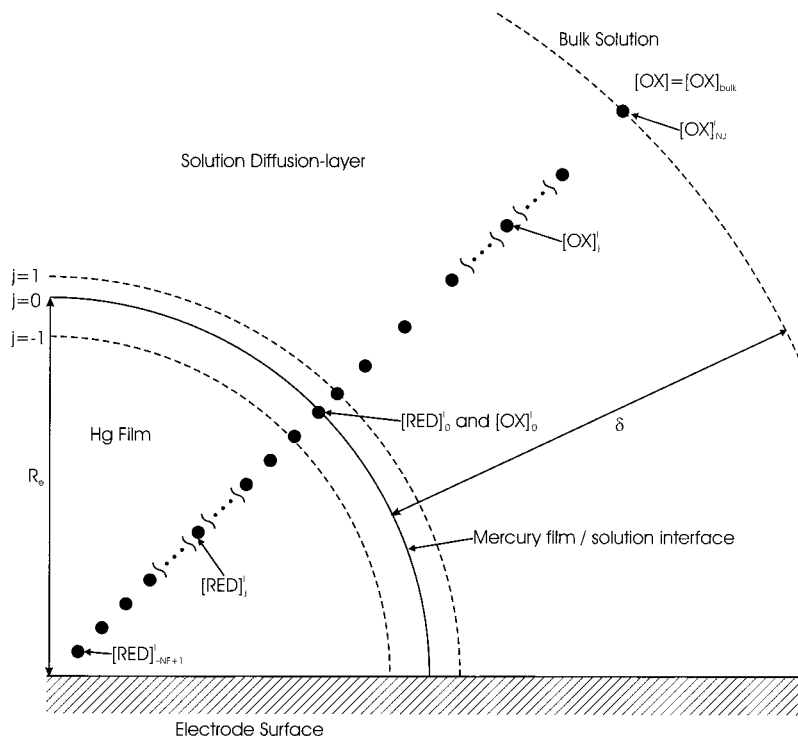$$\varphi = \frac{R_e - R}{R_e} \qquad (14)$$

Figure 3. Schematic diagram showing the spatial node distribution used in the model, for the hemispherical system.

which transforms eq 8 to

$$\frac{\partial a}{\partial t} = \frac{D_a}{R_e^2}\left(\frac{\partial^2 a}{\partial \varphi^2} - \frac{2}{(1-\varphi)}\frac{\partial a}{\partial \varphi}\right) \qquad (15)$$

This is valid for $0 \leq \varphi \leq 1$ (i.e., where $0 \leq R \leq R_e$). This gives rise to evenly spaced grid nodes (see Figure 3).

A back-to-back grid[11−13] based on the coordinates ψ and φ is introduced. The grid is defined such that negative spatial node labels, where the coordinate φ operates, are used to simulate RED species, and positive values, where the coordinate ψ operates, for OX species. The electrode surface is placed at $R = R_e$, corresponding to the node label zero, and a finite diffusion layer boundary at $R = R_e + \delta$ (δ is defined as the thickness of the diffusion layer). Equations 13 and 15 can be simply cast into finite difference form, the first step in the backward implicit method,[14,15] to give

$$a_j^{l-1} = (\lambda_{2a,j} - \lambda_{1a})a_{j-1}^l + (1 + 2\lambda_{1a})a_j^l - (\lambda_{1a} + \lambda_{2a,j})a_{j+1}^l \qquad (16)$$

$$b_j^{l-1} = -\lambda_{b,j}b_{j-1}^l + (1 + 2\lambda_{b,j})b_j^l - \lambda_{b,j}b_{j+1}^l \qquad (17)$$

where l is the temporal node label in a single pulse, separated by a time, Δt, and j is the spatial node label, separated by distance

$$\Delta\psi = \frac{\delta}{(R_e + \delta)NJ} \qquad (18)$$

$$\Delta\varphi = \frac{1}{NF} \qquad (19)$$

NF is the number of node points in the film and NJ the number of node points in solution. The coefficients have the following definitions

$$\lambda_{1a} = \frac{D_a\Delta t}{R_e^2(\Delta\varphi)^2} \qquad (20)$$

$$\lambda_{2a,j} = \frac{D_a\Delta t}{RR_e\Delta\varphi} = \frac{D_a\Delta t}{(1-\varphi_j)R_e^2\Delta\varphi} \qquad (21)$$

$$\lambda_{b,j} = \frac{D_b\Delta t(1-\psi_j)^4}{R_e^2(\Delta\psi)^2} \qquad (22)$$

At the start of SWV experiment, the concentration of the reduced species is at its initial value, while that of OX is very close to zero. Hence the following boundary conditions apply. At $t = 0$

for $R > R_e \quad b = 0$

for $0 < R < R_e \quad a = 1$

At the electrode surface the flux of OX and RED species is conserved, and its magnitude depends on diffusion as well as the rate of kinetic interconversion. These considerations generate further boundary conditions, and using eq 1 it follows that

$$D_a\frac{\partial a}{\partial R}|_{R=R_e} = D_b\frac{\partial b}{\partial R}|_{R=R_e} \qquad (23)$$

$$-D_a\frac{\partial a}{\partial R}|_{R=R_e} = -k_b^a\{b_0^l - a_0^l e^\theta\} \qquad (24)$$

Conversion of eq 23 into finite-difference form gives

$$D_a\frac{(a_0 - a_{-1})}{\Delta\varphi} = D_b\frac{(b_1 - b_0)}{\Delta\psi} \qquad (25)$$

Combining eq 24 and eq 25 gives explicit solutions for either a_0 or b_0 in terms of a_{-1} and b_1 as follows

$$a_0 = k_{a1}a_{-1} + k_{a2}b_1 \qquad (26)$$

Anodic Stripping Voltammetry at Hg-Plated Electrodes

J. Phys. Chem. B, Vol. 104, No. 34, 2000 **8271**

SCHEME 1: Matrix Equation

$$
\begin{bmatrix}
[\text{RED}]^{t-1}_{-\text{NF}+1} \\
\vdots \\
[\text{RED}]^{t-1}_{-2} \\
[\text{RED}]^{t-1}_{-1} \\
[\text{OX}]^{t-1}_{1} \\
[\text{OX}]^{t-1}_{2} \\
\vdots \\
[\text{OX}]^{t-1}_{\text{NJ}-1}
\end{bmatrix}
=
\begin{bmatrix}
1+\lambda_{1a}+\lambda_{2a,-\text{NF}+1} & -\lambda_{1a}-\lambda_{2a,-\text{NF}+1} & & & & & \\
\lambda_{2a,-2}-\lambda_{1a} & 1+2\lambda_{1a} & -\lambda_{1a}-\lambda_{2a,-2} & & & & \\
 & -\lambda_{1a}+\lambda_{2a,-1} & 1+2\lambda_{1a}-\lambda_{1a}k_{a1}-\lambda_{2a,-1}k_{a1} & -\lambda_{1a}k_{a2}-\lambda_{2a,-1}k_{a2} & & & \\
 & & -\lambda_{b,1}k_{b1} & 1+2\lambda_{b,1}-\lambda_{b,1}k_{b2} & -\lambda_{b,1} & & \\
 & & & -\lambda_{b,2} & 1+2\lambda_{b,2} & -\lambda_{b,2} & \\
 & & & & & -\lambda_{b,\text{NJ}-1} & 1+2\lambda_{b,\text{NJ}-1}
\end{bmatrix}
\cdot
\begin{bmatrix}
[\text{RED}]^{t}_{-\text{NF}+1} \\
\vdots \\
[\text{RED}]^{t}_{-2} \\
[\text{RED}]^{t}_{-1} \\
[\text{OX}]^{t}_{1} \\
[\text{OX}]^{t}_{2} \\
\vdots \\
[\text{OX}]^{t}_{\text{NJ}-1}
\end{bmatrix}
$$

where

$$k_{a1} = \frac{1 + k_b^a \phi_b}{1 + k_b^a \phi_a e^\theta + k_b^a \phi_b}$$

$$k_{a2} = \frac{k_b^a \phi_a}{1 + k_b^a \phi_a e^\theta + k_b^a \phi_b}$$

$$b_0 = k_{b1}a_{-1} + k_{b2}b_1 \tag{27}$$

where

$$k_{b1} = \frac{k_b^a \phi_b e^\theta}{k_b^a \phi_a e^\theta + k_b^a \phi_b + 1}$$

$$k_{b2} = \frac{k_b^a \phi_a e^\theta + 1}{k_b^a \phi_a e^\theta + k_b^a \phi_b + 1}$$

where

$$\phi_a = \frac{R_e \Delta\varphi}{D_a}, \quad \phi_b = \frac{R_e \Delta\psi}{D_b}$$

Accordingly, we can handle the normalized concentrations a and b at the electrode surface implicitly. The finite-difference equations at the electrode surface are therefore written as

$$a^{l-1}_{-1} = (-\lambda_{1a} + \lambda_{2a,-1})a^l_{-2} + (1 + 2\lambda_{1a} - \lambda_{1a}k_{a1} - \lambda_{2a,-1}k_{a1})a^l_{-1} - (\lambda_{1a}k_{a2} + \lambda_{2a,-1}k_{a2})b^l_1 \tag{28}$$

$$b^{l-1}_1 = -\lambda_{b,1}k_{b1}a^l_{-1} + (1 + 2\lambda_{b,1} - \lambda_{b,1}k_{b2})b^l_1 - \lambda_{b,1}b^l_2 \tag{29}$$

Far from the electrode (at $R_e + \delta$) the concentration of the oxidized species tends to its bulk value of zero, while at $R = 0$ there is a no flux boundary for the reduced species. These requirements provide the following boundary conditions

$$a^{l-1}_{-nf+1} = (1 + \lambda_{1a} + \lambda_{2a,-nf+1})a^l_{-nf+1} - (\lambda_{1a} + \lambda_{2a,-nf+1})a^l_{-nf+2} \tag{30}$$

All the relevant equations may now be grouped together to

$$b^{l-1}_{nj-1} = -\lambda_{b,j}b^l_{nj-2}(1 + 2\lambda_{b,j})b^l_{nj-1} \tag{31}$$

form a single matrix equation, shown in Scheme 1. This tridiagonal matrix is solvable using the Thomas algorithm.[16−20] The solution provides the full concentration profile of both species as a function of time throughout the experiment.

The flux of species being oxidized is given by eq 1. This in turn allows the current to be calculated, so by comparison with eq 24

$$I = nFAj = nFAD_a\frac{(a_{-1} - a_0)}{R_e\Delta\varphi}[\text{RED}]_{t=0} \tag{32}$$

where the value of a_0 is given by eq 26 and a_{-1} is generated by the simulation. To correspond with experimental practice, the difference current ΔI is recorded. This is calculated (eq 7) by subtracting the simulated backward current $I(2)$ from the simulated forward current $I(1)$: these two currents are calculated using eq 32 at the points in the pulse shown in Figure 1.

A variation to the simulation is to consider the limit where the electrode process is totally irreversible; that is, no reduction at all occurs at the electrode surface. The electrode process becomes

$$\text{RED(amalgam)} \xrightarrow{k_f} \text{OX(aq)} + 2e^- \tag{33}$$
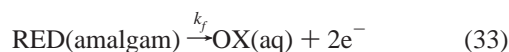
This can be simulated by simplifying eq 1 to

$$j = k_b^a[\text{RED}]e^\theta \tag{34}$$

which modifies eqs 26 and 27 to

$$a_0 = k_{a1}a_{-1} \tag{35}$$

$$k_{a1} = \frac{1}{1 + k_b^a \phi_a e^\theta}$$

and

$$b_0 = k_{b1}a_{-1} + b_1 \tag{36}$$

$$k_{b1} = \frac{k_b^a \phi_b e^\theta}{k_b^a \phi_a e^\theta + 1}$$

Uniform Thin Film. We can model a uniform thin film by considering, rather than a hemisphere of mercury, an electrode consisting of a thin film of mercury on the outside of an inert hemispherical center (Figure 2b). When the radius of the inert center is large, $R_e \to \infty$, the system will be equivalent to a uniform planar electrode. This will allow for comparison with previous work,[21,22] and for contrast with the hemispherical case developed above.

The derivation is mostly the same as for the hemispherical electrode system described above. However, the reduced species does not exist in the region of $0 \le R \le R_e$ but in the range $(R_e - m) \le R \le R_e$, where m is the thickness of the mercury film. R_e remains the radius of the surface of the mercury film.

Accordingly, we modify eq 19 to become

$$\Delta\varphi = \frac{m}{R_e \cdot \text{NF}} \tag{37}$$

All other equations remain the same.

8272 *J. Phys. Chem. B, Vol. 104, No. 34, 2000*

Powell et al.

TABLE 1: Deposition Times and Potentials Used for Carrying Out the Mercury Plating

substrate material	deposition time (s)	deposition potential (V) (vs SCE)
iridium	60	0.0
	120	0.0
	360	0.0
copper	10	−1.0

Computation. All programs were written in FORTRAN 77 and executed on a Silicon Graphics origin 2000 server. Results were analyzed using Microsoft Excel 7.0 or IDL 5.0. The simulations were converged to 1% (as estimated by comparison with a number of "overconverged" runs covering the range of parameters investigated). Typical values of NJ = 4000, NF = 1000, nodes = 500 (where nodes is the number of time nodes per pulse) were found to be appropriate.

Experimental Section

Apparatus. The electrochemical deposition experiments were performed using either a computer-controlled PGSTAT20 Autolab potentiostat (Eco-Chemie, Utrecht, Netherlands) or a μAUTOLAB (Eco-Chemie, Utrecht, Netherlands). All experiments were carried out in a previously described electrochemical cell,[18] employing a platinum coil as an auxiliary electrode and a saturated calomel electrode, SCE, as the reference electrode (Radiometer, Copenhagen, Denmark). Atomic force microscopy, AFM, measurements were conducted using a TopoMetrix TMX 2010 Discoverer system operating in contact mode (10 Hz scan rate). Pyramidal silicon nitride tips (TopoMetrix AFM PROBES 1520) were employed. Images were obtained ex situ, after the electrode substrate had been treated as explained further below.

Reagents. Reagents used were mercury(II) perchlorate hydrate (98%) and perchloric acid (70% A.C.S.), both supplied by Aldrich (Poole, Dorset, UK). Solutions were prepared using UHQ grade water of resistivity not less than 18 MΩ cm^{-1} (Elgastat, High Wycombe, Bucks., UK).

Experimental Procedure. A 1 mm diameter iridium electrode and a 5 mm diameter copper electrode, each mounted in a Teflon support, were used as substrates for mercury deposition experiments. Prior to each experiment, the electrodes were polished using diamond pastes of progressively finer particle size down to 1 μm (Kemet, Kent, UK) and rinsed with UHQ water.

Literature reports of mercury plating of iridium and copper have appeared.[24,25] Thus, the iridium electrode was plated with mercury using 250 mL of a mercury plating solution,[25] consisting of 0.02 M perchloric acid and 0.1 M mercury(II) perchlorate, by holding the potential of the working electrode at 0.00 V (vs SCE) for various deposition times. The copper electrode was plated in a voltammetric cell containing 100 mL of a mercury plating solution, consisting of 0.03 M perchloric acid and 0.003 M mercury(II) perchlorate. Plating was carried out by holding the potential of the working electrode at −1.00 V (vs SCE) for various lengths of time and immediately removing the electrode from the solution after plating was complete.

After removal from the solution, the electrode was rinsed with UHQ water and AFM images were obtained. Imaging was carried out with each metal for a number of different deposition times. In the copper electrode case, some further AFM images were recorded 24 h later to see if the nature of the surface had changed.
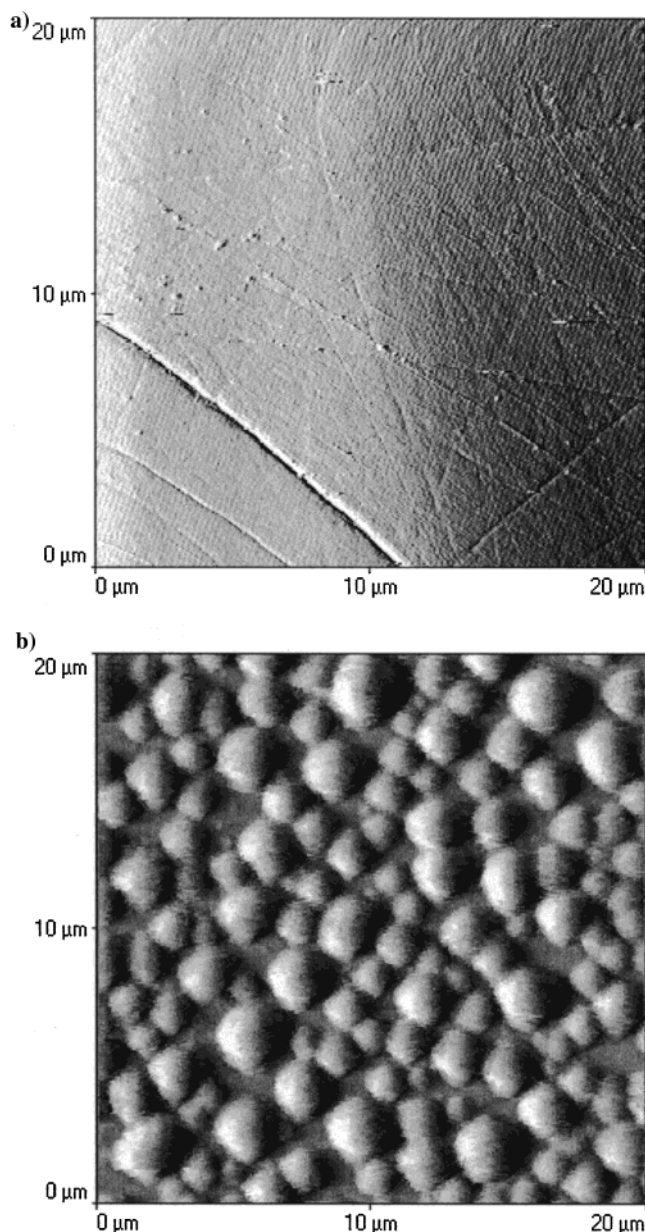

Figure 4. Ex situ AFM images of (a, top) a polished iridium electrode, (b, bottom) same electrode as in (a) after 360 s of mercury deposition at 0.0 V.

Experimental Results and Discussion

The effect of mercury plating copper and iridium electrodes was investigated using AFM imaging. A number of different deposition times were used as shown in Table 1. The resulting AFM images are shown in Figures 4 and 5. Uncoated electrodes are also shown for comparison. The image in Figure 4b shows the presence of droplets on iridium. Droplets were formed over a large range of deposition times, although the range of sizes observed varied; the droplets ranged from 0.5 to 1.0 μm in diameter after 60 s deposition time, from 0.5 to 1.2 μm after 120 s, and from 1.0 to 2.5 μm after 360 s deposition time.

Repeated scanning of an area 10 μm square showed that the mercury droplets reduced in size, possibly due to the AFM tip removing the mercury. A 20 μm square area was then scanned that contained the original area, and it was visible that the droplets had been largely removed in the area that had been repeatedly scanned, supporting the interpretation that they were indeed droplets of mercury.
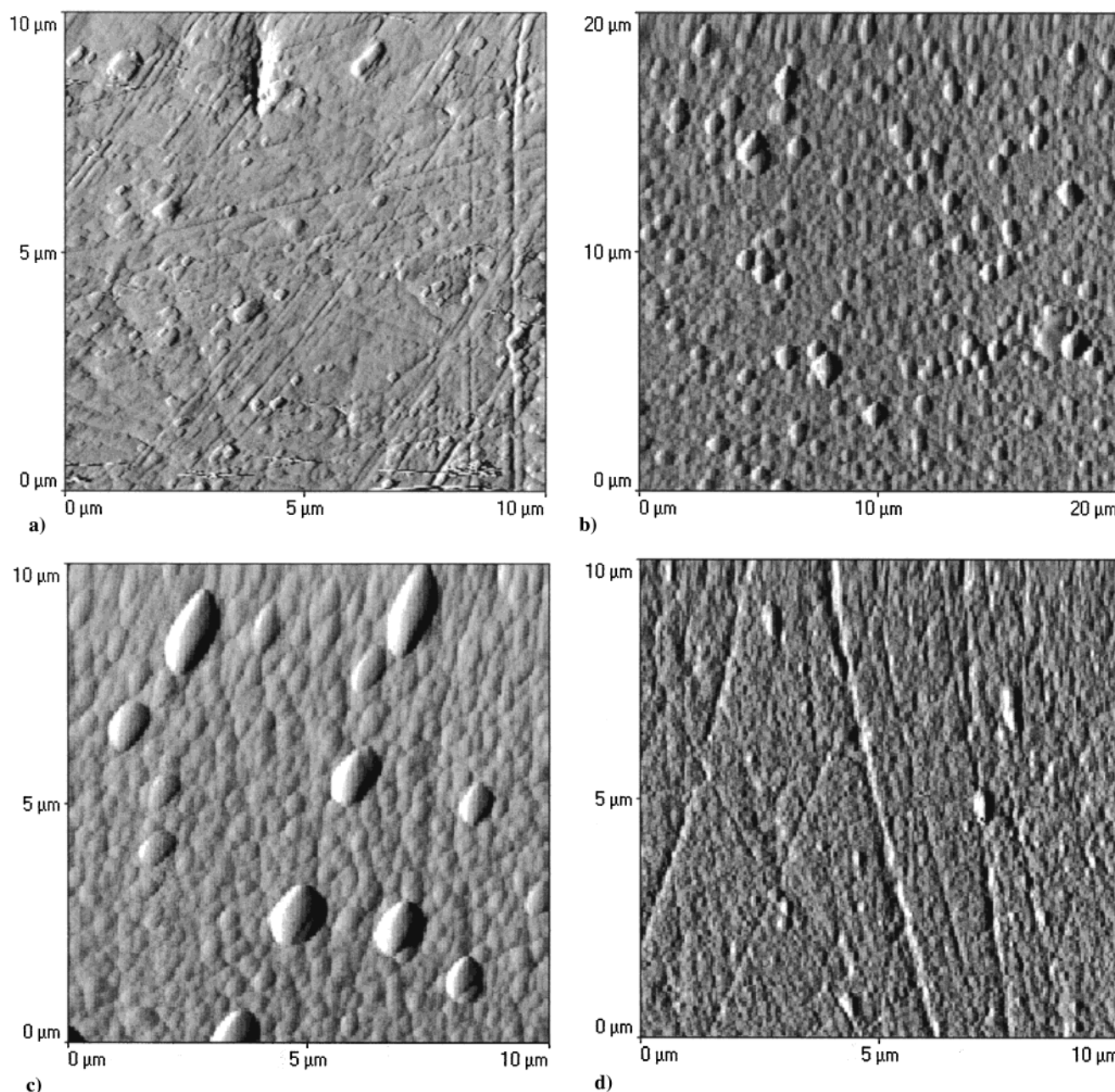
Anodic Stripping Voltammetry at Hg-Plated Electrodes

J. Phys. Chem. B, Vol. 104, No. 34, 2000 **8273**

Figure 5. Ex situ AFM images of (a) a polished copper electrode, (b) and (c) same electrode as in (a) after 10 s of mercury deposition at −1.0 V, and (d) the same mercury plated copper electrode as in (b) and (c) after 24 h stored in UHQ water.

The images in Figure 5b,c show the presence of droplets, typically with a diameter of 0.8−1.2 μm, on the surface of copper. It is noted from the phase diagram of the Cu−Hg system[26,27] that the phase consisting of mercury with some dissolved copper is unstable with respect to a copper−mercury alloy, and ultimately in the presence of excess copper this alloy is unstable with respect to mercury dissolved in copper. A significant change in the nature of the surface is evident in Figure 5d, this AFM being recorded 24 h after the deposition was carried out.

The AFM images in both Figures 4 and 5 provide firm support for the existence of mercury in the form of approximately hemispherical droplets rather than a continuous film, under certain conditions, on both iridium and copper substrates. Accordingly we next turn to the results of the simulations to predict the effects of surface morphology on the voltammetric response to the square wave anodic stripping experiment.

Theoretical Results and Discussion

Validation. We consider first the results obtained for transport to a planar electrode (simulated using an inert center system with $R_e = 1000$ μm) under conditions of semiinfinite diffusion noting that this limit has been explored via simulation by Ball and Compton[21] and analytically by Kounaves et al.[22] for the case of electrochemically reversible systems. A value of $A_1 = 10$ cm s^{-1} was chosen to simulate the electrochemically reversible limit. Voltammograms were obtained for a range of values of film thickness, from $m = 0.03$ μm to $m = 300$ μm, and the characteristic peak shift (the voltage at which the peak in the voltammogram occurs measured relative to $E^{\circ\prime}$) value recorded in each case. The film thickness values and other parameters were chosen to duplicate Figure 4 in ref 21. The satisfying correlation with the literature of simulated values of peak shift versus log Λ, where Λ is[21,22]

$$\Lambda = m\left(\frac{f}{D_a}\right)^{1/2} \tag{38}$$

can be seen in Figure 6, where f is the frequency in hertz. Similarly, voltammograms for a range of values of nE_{SW}, from 1 to 100 mV, were simulated and characteristic peak shift and peak widths (the width of the voltammogram peak at half its maximum height) recorded, to replicate Table 1 in ref 22. The excellent agreement is shown in Figure 7. The ability to quantitatively reproduce results in the literature vindicates both the general method and approach used here and its implementation.

Quasi-Reversible and Irreversible Response of Planar Electrodes. The simulation is not limited to electrochemically reversible systems, but can be readily extended to consider quasi-reversible and irreversible electrode kinetics for various film and diffusion layer thicknesses, for which we are unaware of any previous work. In order to investigate the influence of both the kinetics and film thickness on the square wave ASV, voltammograms were simulated for films of varying thickness ($m = 0.1, 1.0, 3.0, 6.0, 10.0,$ and $16.0\ \mu m$) at a range of different values of A_1 from 1×10^{-5} to 10 cm s^{-1}. For all combinations, simulations were performed where the first step is rate limiting and where the second is rate limiting, using eqs 5 and 6, respectively. Other experimental parameters are given in Table 2. The characteristic peak shift and peak widths of each voltammogram were recorded, and their dependence on film thickness, rate-determining step, and A_1 is shown in Figure 8.

As the value of A_1 is lowered from 10 cm s^{-1} (beyond the totally reversible limit), there is initially no alteration in that characteristic peak shift or peak width, regardless of the film thickness or which step is rate determining (Figure 8a,b). However, when the value of A_1 is dropped below a certain critical value, peak shifts move to increasingly positive potentials. A lower value of A_1 makes both the backward and forward reaction rates smaller, and thus as A_1 is decreased more positive potentials are required to achieve equivalent oxidation rates and consequently the maximum current occurs at a higher potential.

The critical value of A_1 provides the boundary between two distinct regions in the variation of peak shift with A_1. At high A_1 values the peak shift shows no dependence on the rate constant. This is the diffusion-controlled regime. At low A_1 values an increase in peak shift with decreasing A_1 is observed: the (electrode) kinetically controlled region.
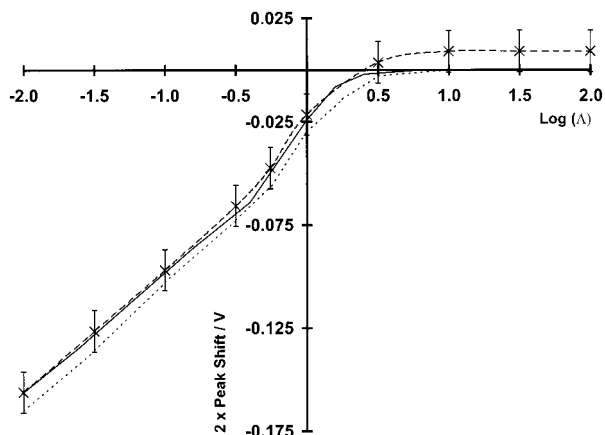

Figure 6. Dependence of the peak shift on log Λ. Other parameters are as discussed in the text. The long dashed line shows the results of the simulation, while the solid line shows the work of Ball and Compton[21] and the short dashed line that of Kounaves and co-workers.[22] The basis of the error bars is discussed in ref 29 and the reason for multiplying peak shift values by two in ref 30.
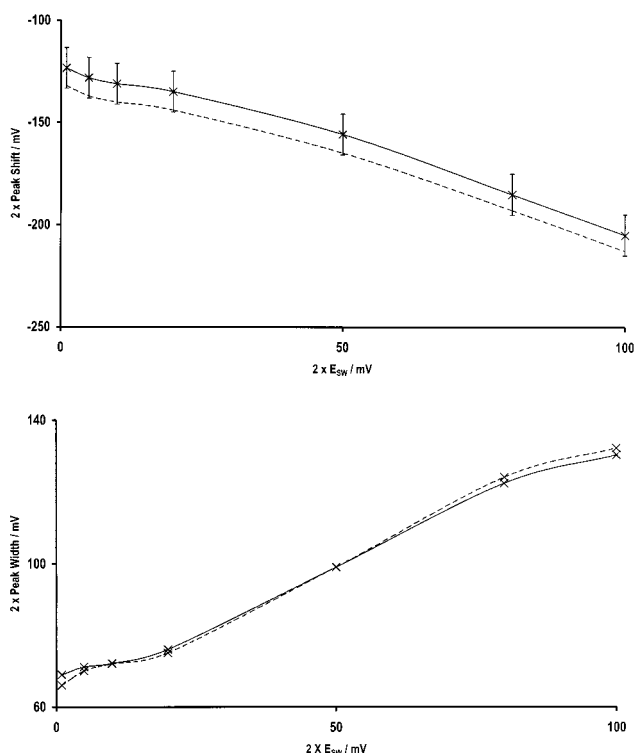

Figure 7. Variation in (a, top) peak shift (the basis of the error bars is discussed in footnote ref 29) with nE_{SW} and (b, bottom) peak width with nE_{SW}. The solid line shows the results of the simulation, while the dashed line shows the work of Kounaves and co-workers.[22] Plotted values are multiplied by two for the reasons discussed in ref 30.

TABLE 2: Parameters Used for the Simulations[a]

parameter	symbol	value	units
electrode radius	R_e	1000.0	μm
diffusion layer thickness	δ	200.0	μm
diffusion constant: reduced species	D_a	1.0×10^{-5} [b]	cm^2 s^{-1}
diffusion constant: oxidized species	D_b	1.0×10^{-5}	cm^2 s^{-1}
rate constant	A_1	10.0	cm s^{-1}
tafel coeffs	$\alpha_1 = \alpha_2$	0.5	
starting voltage of scan	E_i	-1.0	V
finishing voltage of scan	E_f	0.0	V
pulse amplitude	E_{SW}	0.05	V
step voltage of the staircase	ΔE	0.01	V
formal potential of redox couple	$E^{\circ\prime}$	-0.5	V
frequency	f	200	Hz
temp	T	298	K
initial concentration of reduced species	$[RED]_{t=0}$	1.0×10^{-3}	M

[a] These values were used unless another value is specified in the text. [b] This value was used for all calculations except the validation (comparison with results obtained in refs 21 and 22), where the value 2×10^{-5} cm^2 s^{-1} was used.

When a totally irreversible electrode process is simulated, Figure 8a,b, the linear variation of peak shift with the logarithm of the rate constant seen at low A_1 values (the kinetically controlled regime) continues for all values of A_1. This is because the absence of the reverse step means that product materials present near the electrode cannot be converted back into the starting material, and thus their rate of diffusion from the electrode surface is no longer significant. The rate of diffusion of the starting material to the electrode is still important in determining the overall rate of conversion of material, but as this is constant the peak position is now controlled by rate constant as it is this that controls how quickly a equilibrium concentration profile is set up, and thus the position of the peak in the voltammogram.
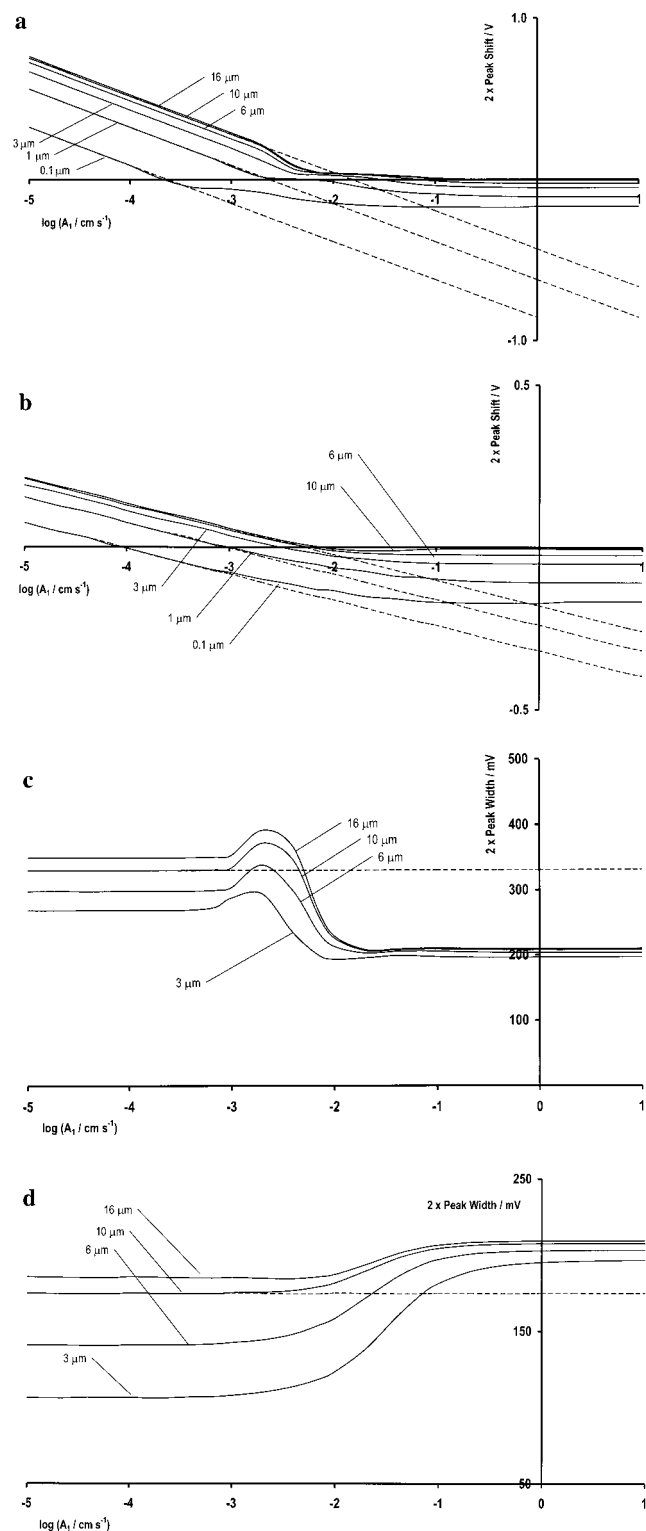
Anodic Stripping Voltammetry at Hg-Plated Electrodes

J. Phys. Chem. B, Vol. 104, No. 34, 2000 **8275**

Figure 8. Simulated results for thin film system: (a) peak shift, first step rate determining (as introduced in text), (b) peak shift, second step rate determining, (c) peak width, first step rate determining, and (d) peak width, second step rate determining as a function of the logarithm of heterogeneous rate constant, A_1. The different lines correspond to mercury films of differing thickness. The solid lines show the results for the quasi-reversible system, while the dashed lines show the results for pure irreversible kinetics (only shown for three of the film thicknesses for clarity).

The peak shift is also observed, Figure 8a,b, to become more positive when the thickness of the electrode is increased. The increased film thickness means there is a larger volume of

mercury, and hence a larger amount of analyte to be oxidized, leading the maximum in the voltammogram to occur at a higher potential.

Another property of the system that the simulation allows us to vary is which of the two electron transfer steps is the rate-determining step (rds). No alteration in peak shift with variation in the rds is observed in the diffusion-controlled regime, as would be expected. The influence of the rds is, however, clearly seen in the kinetically controlled regime where changing the rate-determining process from the first to the second step leads to a decreased dependence of peak shift on the rate constant. This results from more rapid changes in k_b^a close to $E^{\circ\prime}$ when the second step is rate determining. Thus, once the forward pulse potential increases above $E^{\circ\prime}$ so the oxidation occurs more rapidly, and the maximum current occurs closer to $E^{\circ\prime}$ and less variation in the peak shift is observed.

The variations in peak width seen in Figure 8c,d are more complex, each plot showing three distinct regions. There are two regions where peak width is invariant with changes in A_1, at both low and high values of A_1, and an intermediate, more complex region where peak width varies with A_1. The position of this central region corresponds to values of A_1 at the transition between diffusion-controlled and kinetically controlled regimes discussed above.

Examination of Figure 8c,d shows the variation in the peak width as A_1 is reduced from large values corresponding to the diffusion-controlled, electrochemically reversible limit to those pertaining to the kinetically controlled extreme. Interestingly, there is a net increase in peak width on moving from high to low values of A_1 when the first step is rate determining (Figure 8c), but a decrease when the second is the rate determining (Figure 8d). The explanation of this can be most readily appreciated if the square wave voltammograms, together with their individual components $I(1)$ and $I(2)$, are compared with the corresponding linear sweep voltammograms (LSVs). Figure 9 and Figure 10 make these comparisons for the two kinetic cases of interest. Comparison of the LSVs show that there is a progressive broadening of the voltammetric peak on changing from conditions of electrochemical reversibility (Figures 9c and 10c) to the cases where there is kinetic control. If the second step (Figure 10d) is rate determining there is a sharper voltammetric response than the case of the first step being rate determining (Figure 9d) as would be expected from simple Tafel considerations. On examining the SWVs the reversible limit gives rise to the voltammograms seen in Figures 9a and 10a. Note the asymmetry of the peak which is due to the large, 50 mV, amplitude of the square wave (E_{SW}) which leads to a significant $I(2)$ component even at relatively positive potentials. In comparison, Figure 10b, for the case of the second step being rate determining there is a narrowing of the peak largely because the near-IR reversibility of the electrode kinetics shifts the voltammetric feature anodic so that the $I(2)$ component is negligible. In contrast, for the case (Figure 9b) where the first step is rate determining, there remains a significant $I(2)$ component, despite the greater anodic shift, because of the increased sensitivity of the back (reduction) reaction to the electrode potential: this leads to the peak being broadened in comparison with the reversible case.

It is observed that the peak width increases with increasing film thickness (Figure 8c,d), attributable to the larger amount of material to oxidize and the longer time this will take (and hence the greater scan width encompassed in the peak). It is further observed that as expected the peak widths vary more
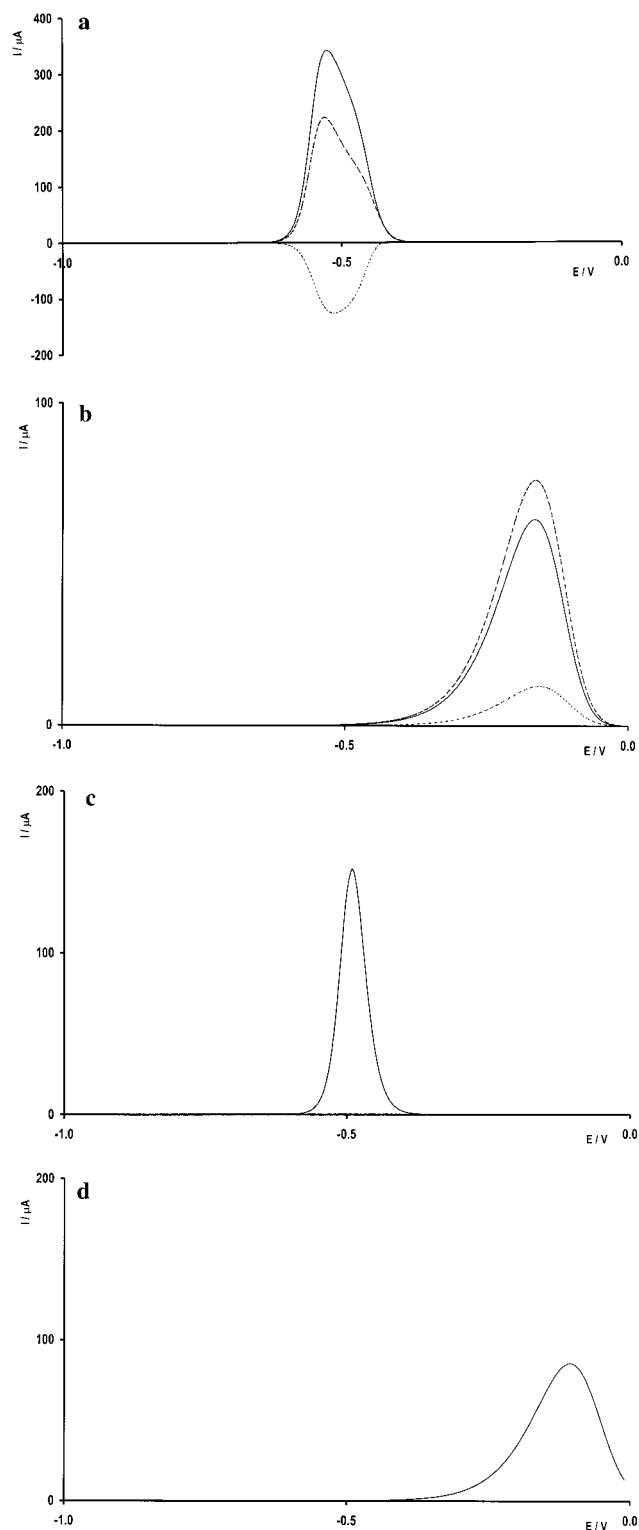
Figure 9. Simulated voltammograms for system with first step rate determining (as introduced in text) for $R_e = 3$ μm and (a) SWV, $A_1 = 10.0$ cm s^{-1}, (b) SWV, $A_1 = 1.0 \times 10^{-5}$ cm s^{-1}, (c) LSV, $A_1 = 10.0$ cm s^{-1}, (d) LSV, $A_1 = 1.0 \times 10^{-5}$ cm s^{-1}. The linear scan voltammograms were obtained by using a modified potential waveform in the simulation.[31]

Figure 10. Simulated voltammograms for system with second step rate determining (as introduced in text) for $R_e = 3$ μm and (a) SWV, $A_1 = 10.0$ cm s^{-1}, (b) SWV, $A_1 = 1.0 \times 10^{-5}$ cm s^{-1}, (c) LSV, $A_1 = 10.0$ cm s^{-1}, (d) LSV, $A_1 = 1.0 \times 10^{-5}$ cm s^{-1}. The linear scan voltammograms were obtained by using a modified potential waveform in the simulation.[31]

with electrode thickness at low heterogeneous rate constants than they do at high A_1 values.

The effect of a totally irreversible electrode process on peak widths is consistent with the behavior of peak shifts; the pattern observed at low values of A_1 continues throughout. That is, the peak width transition 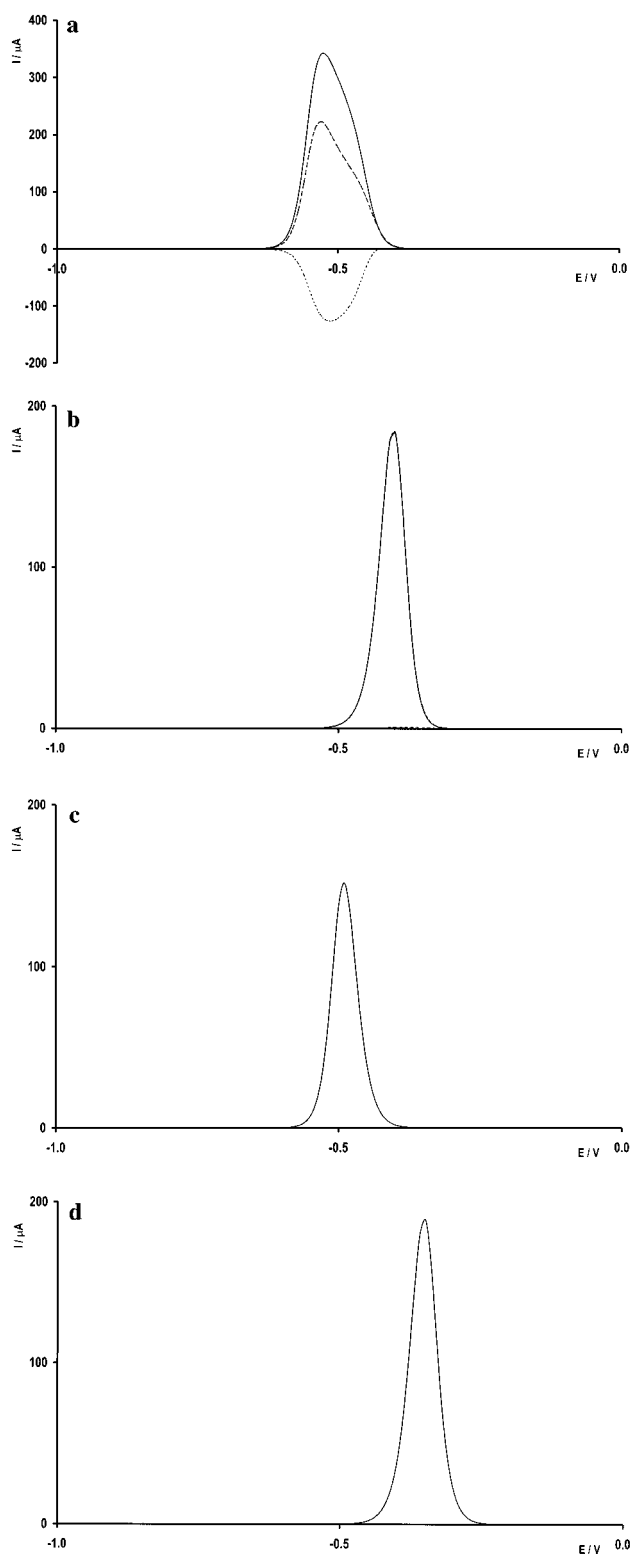from the kinetically controlled to diffusion-controlled characteristic widths is not observed, but the width remains constant at the width characteristic of the kinetically controlled system, as diffusion of products away from the electrode is no longer a limiting factor.

Anodic Stripping Voltammetry at Hg-Plated Electrodes

J. Phys. Chem. B, Vol. 104, No. 34, 2000 **8277**

Hemispherical Electrodes. The simulation allows the modeling of a hemispherical electrode system. We are unaware of any previous work describing square wave ASV for this electrode geometry. To investigate the influence of both the kinetics and electrode radius on the square wave ASV for this system, characteristic voltammograms were again simulated and characteristic peak shift and peak width values recorded. The results of simulations of several electrode radii (R_e = 0.1, 1.0, 3.0, 6.0, 10.0, and 16.0 μm) at a range of different values of A_1 from 1×10^{-5} to 10 cm s^{-1}, for systems where both the first and second step are rate determining (other experimental parameters are given in Table 2), can be seen in Figure 11.

The broad trends are qualitatively similar to those observed for the inert centered system discussed above, but the quantitative details differ significantly. The diffusion and kinetic control regimes are still present, as is the increase in peak shift value with decreasing A_1, below a critical value of A_1 (the quasi-reversible region) and at all values of A_1 in the totally irreversible limit.

It is observed that the peak shift potential increases with increasing electrode radius, as a result of the increased amount of analyte (Figure 11a,b). However, there is a greater dependency of peak shift on variation in the electrode radius than with an equivalent variation in the film thickness in the inert centered electrode case. This results in part from a more marked increase in the volume of mercury, and hence analyte, with electrode radius in the hemispherical case (doubling the diameter of the hemispherical electrode causes the volume of mercury to go up 8-fold, but increasing the film thickness in the inert centered cases has a much smaller effect on the volume of mercury as it is around a large inert center), but also from the enhanced mass transport at the hemispherical electrode.

Peak widths again show three distinct regions, reducing to the peak width being invariant with A_1 in the totally irreversible limit, but there are marked differences. In the inert center case there is a net decrease in peak width on moving to higher values of A_1 when the first step is the rate determining (Figure 8c), and an increase when the second step is the rate determining (Figure 8d). The hemispherical system, however, is more interesting. It again shows a decrease when the first step is rate determining (Figure 11c), but the relative widths lead to a spreading out of peak width with increasing A_1 when the second step is rate determining (Figure 11d).

In all cases, for both electrode geometries, the peak width increases with increasing electrode diameter/film thickness,[28] attributable to the larger amount of material to oxidize (and hence the greater scan width encompassed in the peak). However, while the peak widths increase more with electrode thickness, in the inert center case, at low values of A_1 than they do at high A_1 values (Figure 8c,d), the opposite is true in the case of the hemispherical system (Figure 11c,d). In the kinetically controlled limit for the hemispherical system, with increasing radius there is also a large increase surface area for electrode reaction. So although there is an increase in the amount of material to oxidize and a reduction in the enhanced mass transport, there is also an increase in surface area at which this kinetically limited process can be carried out, hence minimizing the increase in peak width with increase in electrode radius. In the system with an inert center, the change in surface area is less relative to the volume, since an alteration in the film thickness only has a small effect on the overall radius of the electrode, and so the dependence of peak width on film thickness is greater. In the diffusion-controlled limit of the hemispherical system, the peak width increases rapidly with electrode radius
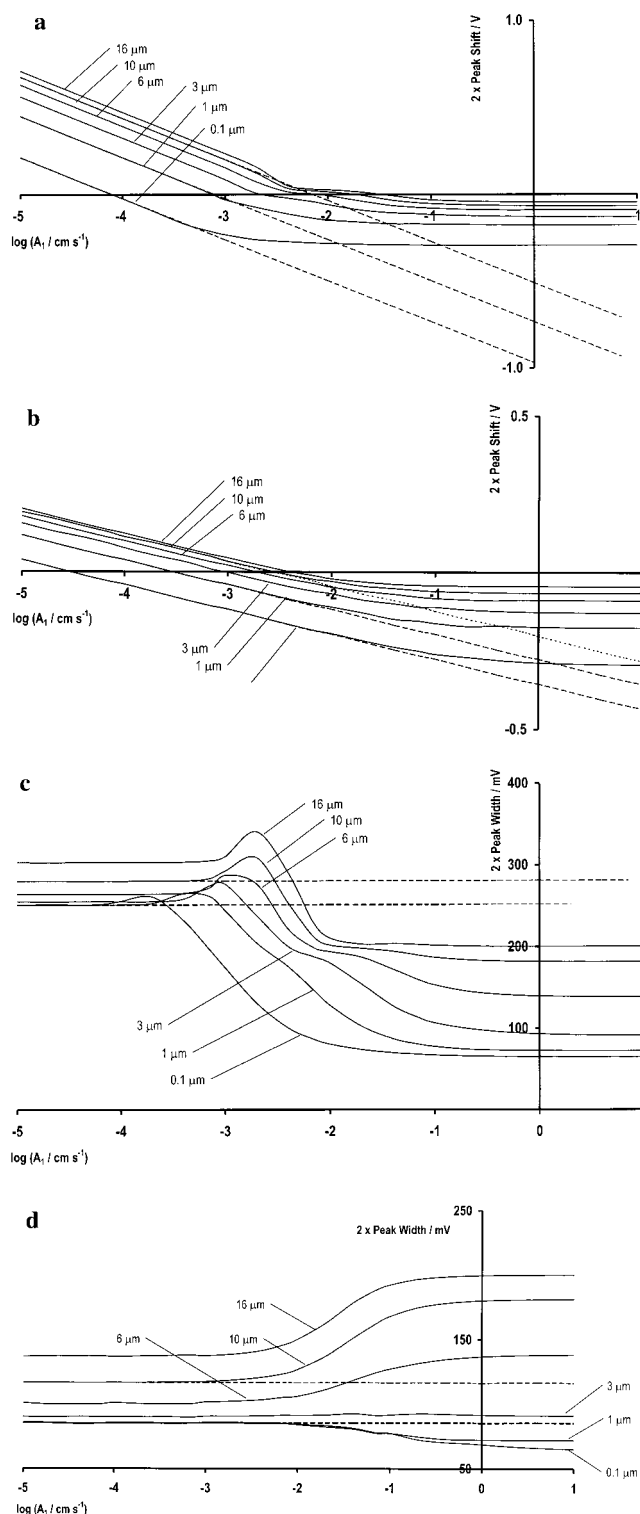
Figure 11. Simulated results for droplet system: (a) peak shift, first step rate determining (as introduced in text), (b) peak shift, second step rate determining, (c) peak width, first step rate determining, (d) peak width, second step rate determining as a function of the logarithm of heterogeneous rate constant, A_1. The different lines correspond to mercury hemispheres of differing radius. The solid lines show the results for the quasi-reversible system, while the dashed lines show the results for pure irreversible kinetics (only shown for three of the electrode radii for clarity).

due to the equally sharp increase in material available for oxidation and decrease in the enhanced mass transport, whereas the effect of film thickness in the inert center case is less marked

as the electrode is already of substantial radius. Further trends are also visible in the peak width variation.

First, the peak widths show a greater variation with changes in electrode radius in the hemispherical system than for an equivalent variation in the film thickness of the inert centered system, as was observed with the peak shift and for the same reasons.

Second, with increasing electrode radius the enhanced mass transport that exists to the hemispherical electrode is depleted, and the diffusion become increasingly like that to a uniform film. Consequently, both the characteristic peak widths, and peak shifts, of the inert centered and hemispherical systems tend to the same value as the electrode radius/film thickness[28] is increased.

Conclusions

AFM evidence of mercury existing as droplets of mercury on both iridium and copper substrates, under certain conditions, has been presented. Simulations of square wave ASV at hemispherical electrodes have been produced for reversible, irreversible, and quasi-reversible redox couples. The simulation of square wave ASV at uniform thin films has been extended, from the reversible limit, to encompass irreversible and quasi-reversible redox couples. The simulations have revealed significant quantitative differences between the behavior at electrodes of these two geometries. Moreover, the value of simulations in facilitating the understanding of the voltammetric responses, as illustrated for example by the generation of Figures 9 and 10 in respect of gaining insight into Figure 8, is again evident.

References and Notes

(1) Štulíková, M. *J. Electroanal. Chem.* **1973**, *48*, 33.

(2) Wu, H. P. *Anal. Chem.* **1994**, *66*, 3151.

(3) Zakharchuk, N. F.; Brainina, K. Z. *Electroanalysis* **1998**, *10*, 379.

(4) Akkermans, R. P.; Ball, J. C.; Marken, F.; Compton, R. G. *Electroanalysis* **1998**, *10*, 26.

(5) Kruijt, W. S.; Sluyters-Rehbach, J. H.; Sluyters, J. H.; Milchev, A. *J. Electroanal. Chem.* **1994**, *371*, 13.

(6) Kounaves, S. P.; Deng, W. *J. Electroanal. Chem.* **1991**, *301*, 77.

(7) Kounaves, S. P.; Buffle, J. *J. Electroanal. Chem.* **1987**, *216*, 53.

(8) Van Venrooij, T. G. J.; Sluyters-Rehbach, M.; Sluyters, J. H. *J. Electroanal. Chem.* **1996**, *419*, 61.

(9) Alden, J. A.; Hutchinson, F.; Compton, R. G. *J. Phys. Chem. B.* **1997**, *101*, 949.

(10) Amatore, C.; Fosset, B. *Anal. Chem.* **1996**, *68*, 4377.

(11) Dryfe, R. A. W. D.Phil. Thesis, Oxford University, 1995; p 82.

(12) Bidwell, M. J.; Alden, J. A.; Compton, R. G. *J. Electroanal. Chem.* **1996**, *417*, 119.

(13) Alden, J. A.; Compton, R. G. *J. Phys. Chem. B* **1997**, *101*, 8941.

(14) Anderson, J. L.; Moldoveanu, S. *J. Electroanal. Chem.* **1984**, *179*, 107.

(15) Compton, R. G.; Pilkington, M. B. G.; Stearn, G. M. *J. Chem. Soc., Faraday Trans. 1* **1988**, *84*, 2155.

(16) Thomas, L. H. *Elliptical problems in linear equations over a network*, Watson Sci. Comput. Lab. Rep., Columbia University, New York, 1949.

(17) Laasonen, P. *Acta Math.* **1949**, *81*, 30917.

(18) Bruce, G. H.; Peaceman, D. W.; Rachford, H. H.; Rice, J. D. *Trans. Am. Inst. Min. Engr.* **1953**, *198*, 79.

(19) Fisher, A. C.; Compton, R. G. *J. Phys. Chem.* **1991**, *95*, 7538.

(20) Fisher, A. C.; Compton, R. G. *J. Appl. Electrochem.* **1992**, *22*, 38.

(21) Ball, J. C.; Compton, R. G. *J. Phys. Chem. B* **1998**, *102*, 3967.

(22) Kounaves, S. P.; O'Dea, J. J.; Chandresekhar, P.; Osteryoung, *J. Anal. Chem.* **1987**, *59*, 386.

(23) Compton, R. G.; Eklund, J. C.; Page, S. D. *J. Phys. Chem.* **1995**, *99*, 4211.

(24) Daly, P. J.; Page, D. J.; Compton, R. G. *Anal. Chem.* **1983**, *55*, 1191.

(25) Wang, J.; Wang, J.; Tian, B.; Jiang, M. *Anal. Chem.* **1997**, *69*, 1657.

(26) Chakrabarti, D. J.; Laughlin, D. E. *Bull. Alloy Phase Diagrams* **1985**, *6*, 522.

(27) Lugscheider, E.; Gerhard, J. *Z. Metallk.* **1971**, *62*, 548.

(28) Thickness applies to the thickness of mercury, outside the inert center, in the case of the pseudo thin film electrode system, and electrode diameter applies to the diameter of the hemisphere of mercury in the hemispherical system.

(29) The error bars in Figure 6 arise from the fact that the voltage steps in the simulation are of 5 mV amplitude so that the potential shift values associated with any value of Λ have a maximum uncertainty of this size. For all the points the predictions of the previous work lie within the error bars.

(30) All plotted values of peak shift, peak width, and square wave amplitude are shown multiplied by two (where two is the number of electrons transferred in the redox couple being simulated). This is done for consistency with the literature,[21,22] where values are plotted, for example, as nE_{SW}.

(31) Ball, J. C.; Compton, R. G. *Electroanalysis* **1997**, *9*, 1305.